

## Microstructure–Property Correlations in Industrial Thermal Barrier Coatings

Anand A. Kulkarni,\* Allen Goland, and Herbert Herman

Department of Materials Science and Engineering, State University of New York, Stony Brook, New York 11794

Andrew J. Allen,\* Jan Ilavsky,\* and Gabrielle G. Long\*

National Institute of Standards and Technology, Gaithersburg, Maryland 20899

Curtis A. Johnson\* and Jim A. Ruud\*

General Electric Corporate Research Division, Schenectady, New York 12309

**This paper describes the results from multidisciplinary characterization/scattering techniques used for the quantitative characterization of industrial thermal barrier coating (TBC) systems used in advanced gas turbines. While past requirements for TBCs primarily addressed the function of insulation/life extension of the metallic components, new demands necessitate a requirement for spallation resistance/strain tolerance, i.e., prime reliance, on the part of the TBC. In an extensive effort to incorporate these TBCs, a design-of-experiment approach was undertaken to develop tailored coating properties by processing under varied conditions. Efforts focusing on achieving durable/high-performance coatings led to dense vertically cracked (DVC) TBCs, exhibiting quasi-columnar microstructures approximating electron-beam physical-vapor-deposited (EB-PVD) coatings. Quantitative representation of the microstructural features in these vastly different coatings is obtained, in terms of porosity, opening dimensions, orientation, morphologies, and pore size distribution, by means of small-angle neutron scattering (SANS) and ultra-small-angle X-ray scattering (USAXS) studies. Such comprehensive characterization, coupled with elastic modulus and thermal conductivity measurements of the coatings, help establish relationships between microstructure and properties in a systematic manner.**

### I. Introduction

COMPREHENSIVE efforts have been under way to incorporate prime-reliant and energy-efficient ceramic thermal barrier coatings (TBCs) into advanced gas turbine and diesel engine components. TBCs provide insulation to metallic structures in the hot section of land-based/aero-turbine engines and offer three important benefits: (1) increased operating temperature of the

engine and therefore enhanced efficiency; (2) enhanced durability and extended life of metallic components subjected to high temperatures and high stresses; and (3) reduced cooling requirements to metallic components.<sup>1–3</sup> Present-day TBCs are comprised of a two-layer coating system on a superalloy turbine blade substrate. The materials of interest for such systems are MCrAlY (where M is Ni, Co, etc.) alloys or Pt–Al-based oxidation-resistant bond-coats followed by an yttria-stabilized zirconia (YSZ) TBC. The bond-coat is typically deposited using atmospheric or low-pressure plasma spray while the topcoat is deposited using either electron-beam physical vapor deposition (EB-PVD) or plasma spray deposition.<sup>4</sup> Each technique has merits for TBC applications depending on size scale, performance requirements and cost. The EB-PVD process produces a unique columnar microstructure with wide intercolumnar spacing, thus providing superior strain tolerance and thermal shock resistance; hence it is used on rotating airfoils for significant lifetime enhancements. Because plasma-sprayed TBCs produce splat-based layered structures and offer advantages in terms of thermal insulation and economics, they are widely used in combustion chambers. However, such coatings are not considered durable on rotating airfoils due to lack of in-plane compliance that leads to premature delamination failure during thermomechanical cycling under oxidative conditions.<sup>5</sup> This is mainly due to a myriad array of process-related defects in the form of interlamellar pores, cracks, and gas porosity. These imperfections can, to a certain extent, offer beneficial attributes, such as compliance to the coating, enabling high-temperature thermal cycling and reduction of thermal conduction due to phonon scattering, etc.<sup>6</sup> Understanding the characteristics of these defects and their control is critical for the enhancement of the system's performance and reliability.

In plasma spraying, feedstock material is melted and accelerated to high velocities. The resultant melt impinges on the substrate and rapidly solidifies to form a “splat” (a flattened particle). The deposit develops by successive impingement and interbonding among the splats. The microstructure consists of the splats, separated by interlamellar pores resulting from rapid solidification of the lamellae, very fine voids formed by incomplete intersplat contact or around unmelted particles, and cracks due to thermal stresses and tensile quenching stress relaxation.<sup>7,8</sup> Taken together, these imperfections introduce a measurable porosity in the coatings. The cracks increase the compliance of the coating and hence enhance the thermal shock resistance. This microcrack-related feature of YSZ might be exploited to advantage through generation of varying stress states during deposition. Such a microstructure with controlled micro/macrocraacks can yield a compliant TBC coating, which is considered to be beneficial relative to strain tolerance, spallation resistance, and component life during service.<sup>9</sup> Recent efforts on processing/deposition methodologies have

R. Hannink—contributing editor

Manuscript No. 10162. Received April 29, 2004; approved January 24, 2004.

This research was supported by the National Science Foundation (NSF) MRSEC program at the SUNY Stony Brook under Grant No. DMR-0080021. This work used facilities supported in part by the National Science Foundation under Agreement No. DMR-9986442. The UNICAT facility at the Advanced Photon Source (APS) is supported by the University of Illinois at Urbana-Champaign, Materials Research Laboratory (U.S. Department of Energy (DOE), the State of Illinois-IBHE-HECA, and the NSF), the Oak Ridge National Laboratory (U.S. DOE under contract with UT-Battelle LLC), the National Institute of Standards and Technology (U.S. Department of Commerce), and UOP LLC. The APS is supported by the U.S. DOE, Basic Energy Sciences, Office of Science under contract No. W-31-109-ENG-38.

\*Member, American Ceramic Society.

allowed the development of plasma spray processes that produce dense vertically cracked (DVC) TBC microstructures. While the details of the DVC microstructures remain proprietary,<sup>10</sup> studies have clarified that these unique microstructures can be achieved under conditions involving plasma spraying at high power, high powder flow rates, carefully controlled spray distances, and relatively high substrate temperatures (e.g., >400°C).<sup>11–13</sup>

In this paper, advanced scattering techniques to characterize and to compare microstructures of conventional plasma-sprayed coatings with DVCs are explored. Small-angle neutron scattering (SANS) methods have been previously used to characterize and quantify the anisotropic nature of the thermal sprayed ceramic coatings.<sup>14,15</sup> Ultra-small-angle X-ray scattering (USAXS) studies have been conducted in concert to provide quantitative microstructure maps as a function of size of scatterers. This information obtained on porosity, pore size distributions, and pore orientations provides an enhanced understanding that can lead to improvements in coating behavior during service.

## II. Experimental Procedure

### (1) Deposit Properties

Four coatings were studied, each deposited under incrementally different spray conditions onto a NiCrAlY bond-coated superalloy (IN 718) (General Electric, Schenectady, NY).<sup>†</sup> The coatings<sup>1</sup> are labeled GE-1 to GE-4, going from conventional layered structure to DVC, respectively. The coating thickness was ~450 μm in each case. Free-standing coatings were used for porosity determinations, thermal conductivity measurements, and SANS studies. Microstructural evaluation using optical and scanning electron microscopy (SEM) were also conducted. Surface-connected porosity was measured by mercury intrusion porosimetry (MIP) using an Autoscan 33 porosimeter (Quantachrome Corp., Bayton Beach, FL). The total porosity content was determined using the precision density (PD) method, where mass-over-volume ratios were obtained for a cut rectilinear specimen. The technique gives a fractional density (or porosity) uncertainty of standard deviation, ±1%, based on the average of 10 measured identical specimens and an assumed theoretical density of 6 g/cm<sup>3</sup>. Thermal conductivity measurements were conducted on a 12.5 mm (0.5 in.) diameter disk, coated with carbon, using a laser flash thermal diffusivity instrument (Netzsch Corp., Boston, MA). Elastic modulus measurements and USAXS studies were conducted on the coatings bonded to the substrate. Elastic modulus measurements using depth-sensitive indentation studies were conducted with a Nanotest 600 instrument (Micromaterials, Inc., Cambridge, U.K.) with a 1/16 in. WC–Co spherical indenter with a maximum load of 10 N. The instrument enables a basic load/displacement curve to be obtained, or multiple partial load/unload cycles to be performed. This allows hardness and elastic modulus values to be measured as a function of the load/contact stress. The indentation procedure used usually consists of 10–15 loading/unloading cycles. Also, modulus measurements were conducted on polished top-surface (out-of-plane) and cross sections (in-plane) to examine the anisotropy in the coatings.

### (2) Small-Angle Neutron Scattering

SANS studies were conducted on the NIST NSF 30 m NG3 SANS instrument at the Cold Neutron Research Facility at the National Institute of Standards and Technology, Gaithersburg, MD. The use of large sample-to-detector distances on this instrument provides a powerful opportunity to measure the microstructure of thin coatings, which are more representative of industrial applications. This will be the case, provided enough multiple scattering exists for the multiple small-angle neutron scattering (MSANS) formalism to apply. A monochromatic beam of cold

long-wavelength neutrons passes through the specimen in transmission geometry and the scattered neutrons are recorded on a two-dimensional detector. The details of the experiment are described elsewhere.<sup>14,15</sup> The scattering occurs at the void–grain interface due to differences in scattering-length density between the material and the pores. The experiment involved two types of measurements, the first being anisotropic Porod scattering. It is advantageous to measure the Porod scattering since it amplifies the microstructural anisotropies. However, on orientational averaging of the Porod scattering from the sample, one can obtain the total void surface area per unit sample volume, independent of the precise void morphology. The fine features in the microstructure are major contributors to this deduced surface area. The second type of measurement is the anisotropic MSANS, which involves a measurement of the beam-broadening due to anisotropic multiple scattering at long neutron wavelengths (1–1.8 nm). The multiple scattering usually arises from the coarse features in the microstructure. The MSANS beam broadening versus wavelength for two sample orientations, with the incident beam out-of-plane (in the spray direction) and in-plane (i.e., in the substrate plane), yields information on microstructural anisotropy. The sector-averaged anisotropic MSANS data also provide microstructural orientation information, as discussed in detail elsewhere.<sup>15,16</sup>

The goal is to obtain quantitative information on each population of the porosity. This can be obtained by combining MSANS measurements for different sample orientations, anisotropic Porod surface area distributions, and the total porosity found from precision density measurements. To acquire a quantitative delineation of the three void components (interlamellar pores, intrasplat cracks, and globular pores) in terms of their porosity contributions, dimensionality, and orientation distribution, the following four constraints are imposed in the MSANS analysis:

- (1) The component porosities are consistent with the total porosity obtained using precision density measurements.
- (2) The component surface areas are consistent with the total surface area obtained from anisotropic Porod scattering experiments.
- (3) The circularly averaged MSANS beam broadening versus wavelength model predictions are consistent with the experimental data for both orientations: out-of-plane (spray direction) and in-plane (orthogonal direction).
- (4) The predicted MSANS anisotropy (perpendicular to the substrate) is consistent with that observed experimentally.

With these constraints, it is possible to determine the volume-weighted mean-opening dimensions of the intrasplat cracks and interlamellar pores, their orientation distributions with respect to the spray direction, and the diameters of the globular pores. Porosity and surface area contributions may also be distinguished.

### (3) Ultra-Small-Angle X-ray Scattering

Ultra-small-angle X-ray scattering (USAXS) studies were conducted on the UNICAT beam line 33-ID at the Advanced Photon Source, Argonne National Laboratory, Argonne, IL. This instrument uses Bonse–Hart double-crystal optics<sup>17</sup> to extend the range of SAXS to low-scattering vectors,  $\mathbf{Q}$ , where  $\mathbf{Q} = (4\pi/\lambda)(\sin \theta)$  and  $2\theta$  is the scattering angle. In small-angle scattering (SANS and USAXS) studies, the anisotropic structural information is measured along the direction of  $\mathbf{Q}$ . In a modified form of the standard USAXS experiment, a finely collimated and highly monochromatic X-ray beam (prepared using horizontally and vertically diffracting crystals) is incident on the specimen in transmission geometry and scattered intensity is measured. Use of orthogonal diffracting crystals removes the intrinsic slit-smearing geometry of the standard USAXS experiment. The details of the experiment are described elsewhere.<sup>18</sup> The X-ray energy was 17 keV to penetrate through highly absorbing YSZ coatings. Two methods are usually combined. In the first, the scattered intensity is measured as a function of  $\mathbf{Q}$  for each orientation of the azimuthal angle,  $\alpha$ . Alternatively, the scattered intensity at a particular  $\mathbf{Q}$  is measured as a function of  $\alpha$  by rotating the sample in the beam. The different anisotropies in the scattering at different  $\mathbf{Q}$  are related to the

<sup>†</sup>Information on commercial products is given for completeness and does not constitute or imply their endorsement by the National Institute of Standards and Technology.

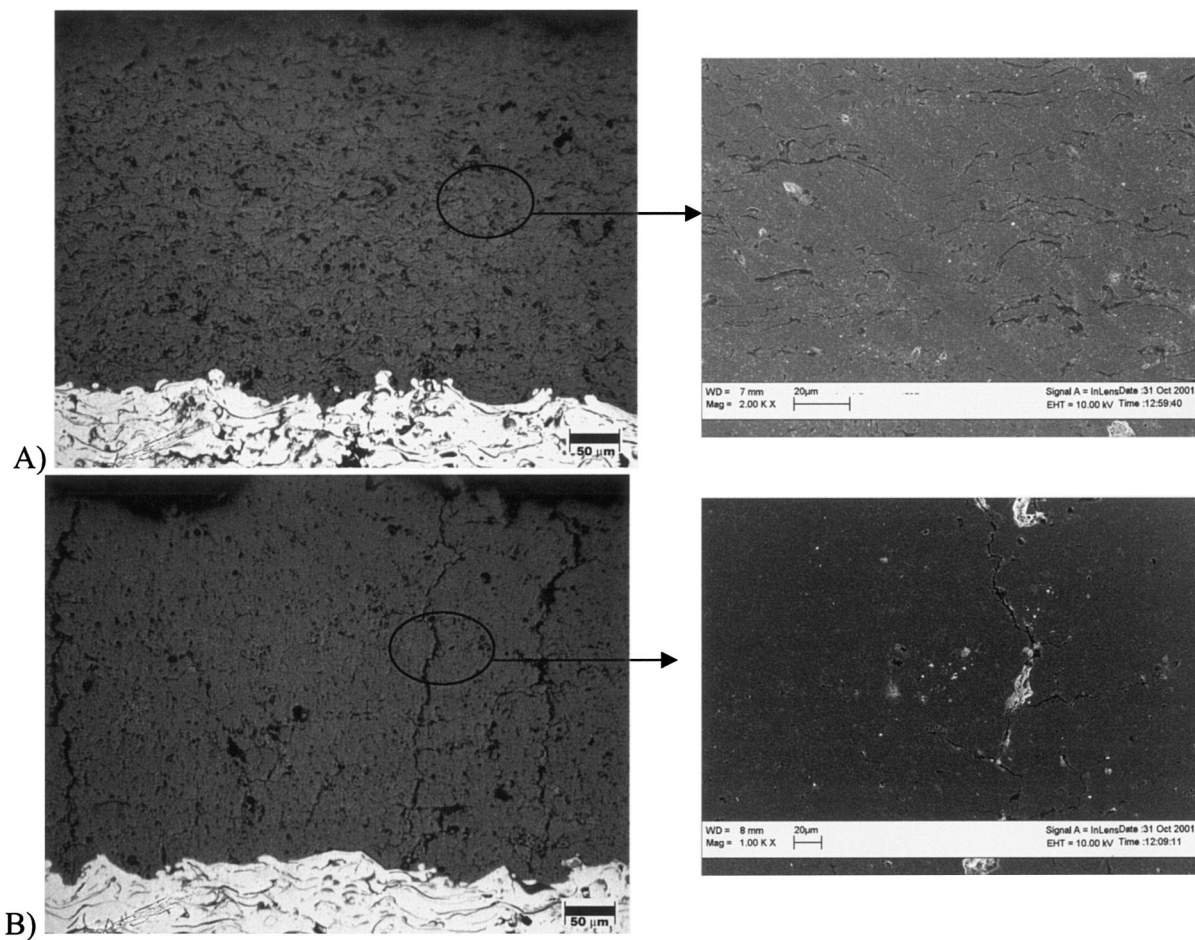


**Fig. 1.** Optical microscopy images of coatings with high-magnification SEM micrographs (on the right) showing detailed microstructure: (A) GE-1 and (B) GE-4.

different anisotropies of the microstructure at different length scales, thus giving a quantitative map as a function of the sizes of the scattering populations. However, the  $Q$  resolution of the instrument limits detection of sizes to those below about 1.5  $\mu\text{m}$  in diameter.

### III. Results and Discussion

The cross-sectional micrographs of the coatings sprayed at the endpoints of incrementally varied conditions (GE-1 and GE-4) are shown in Fig. 1. Figure 1(A) shows a typical plasma-sprayed coating with a layered structure. The interlamellar porosity, which results from poor adhesion between splats, is evident in the inset. Figure 1(B) shows a significantly different structure with vertical macrocracks. These cracks may be beneficial from the point of view of strain tolerance and component life during service. Also, a dense coating structure is observed in the magnified image on the right.

The measured coating properties for the four samples are presented in Table I: density from the precision density method;

porosity from precision density; porosity from mercury intrusion porosimetry (MIP); thermal diffusivity; and conductivity values. The density increases from GE-1 to GE-4 and the MIP surface-connected porosity decreases from GE-1 to GE-3 and then increases for the DVC microstructures (GE-4). This is due to macrocracks being accounted as the surface-connected porosity. The thermal diffusivity and conductivity values measured using the laser flash technique show an inverse relationship with porosity. The elastic modulus measured using depth-sensitive indentation is presented in Fig. 2. In-plane and out-of-plane measurements show anisotropy in these coatings. It is observed that the out-of-plane (top surface) modulus increases consistently similar to the trend of thermal conductivity of the coatings. The in-plane (cross section) modulus, which is sensitive to the crack networks, increases except for the DVC case.

#### (I) SANS Results

SANS results along with MSANS model fits are presented in this section. The anisotropic surface area derived from the Porod scattering regime (Fig. 3) shows the orientation dependence of the

**Table I. Coating Property Measurements**

Coating	Density ( $\text{g}/\text{cm}^3$ )	PD porosity (%)	MIP porosity (%)	Thermal conductivity ( $\text{W}/(\text{m}\cdot\text{K})$ )	Thermal diffusivity ( $\text{cm}^2/\text{s}$ )
GE-1	$5.25 \pm 0.11$	$13.3 \pm 0.7$	$14 \pm 0.3$	$1 \pm 0.1$	$0.005 \pm 0.0006$
GE-2	$5.38 \pm 0.05$	$11 \pm 0.7$	$10 \pm 0.4$	$1.2 \pm 0.04$	$0.009 \pm 0.0004$
GE-3	$5.42 \pm 0.18$	$10.3 \pm 0.6$	$7 \pm 0.6$	$1.7 \pm 0.03$	$0.012 \pm 0.0004$
GE-4	$5.48 \pm 0.28$	$9 \pm 0.5$	$9 \pm 0.5$	$1.9 \pm 0.06$	$0.015 \pm 0.0007$

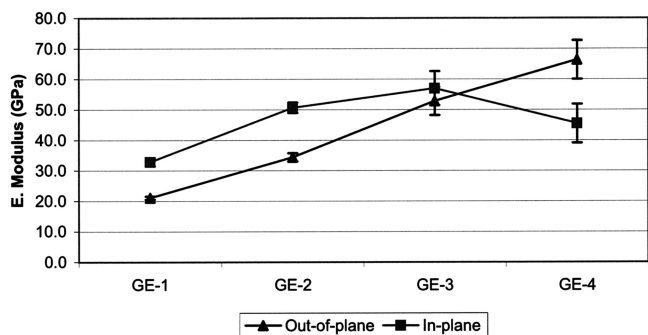


Fig. 2. Comparison of in-plane and out-of-plane elastic properties showing anisotropy in the coatings. Error bars indicate standard deviations for each measurement.

scatterers. Since the scattering data are represented in Fourier space, the contribution from horizontal components is observed vertically and vice versa. It is seen in Fig. 3(A) that the scattering is dominated by horizontal elements (interlamellar pores) in the traditionally plasma-sprayed GE-1 coating. The scattering appears to be crack-dominated in Fig. 3(B) for the GE-4 (DVC) coating.

Since the coatings are deposited by plasma spraying, the microstructure develops by splat-splat layering, suggesting the presence of interlamellar pores in the coating, even though they are not well resolved in the SEM micrograph of Fig. 1(B). The total surface area from the Porod scattering, combined with density/porosity measurements from precision density measurements and MSANS model parameters, together quantify the many details of the microstructure.

Using the constraints in the MSANS model, the results for porosity contributions and mean opening dimensions obtained, are summarized in Table II. Estimated uncertainties are given in parentheses. The incremental changes in the anisotropic orientation distribution of the intrasplat cracks and the interlamellar pores (which are significantly different in the two extreme cases of GE-1 and GE-4) are also shown below in Table II. The orientation distributions for the interlamellar-pore 1/5 aspect ratio spheroidal elements and the intrasplat-crack 1/10 aspect ratio elements are separately parameterized in terms of the relative probabilities of finding the normal to these elements within the range 0–30° from the spray direction, 30–60° from the spray direction, and 60–90° from the spray direction. To obtain good MSANS model fits that satisfy all the constraints, intrasplat cracks are found to be predominantly perpendicular to the substrate (spheroidal-elements normals 60–90° from the spray direction), and the interlamellar pores are found to be predominantly parallel to the substrate

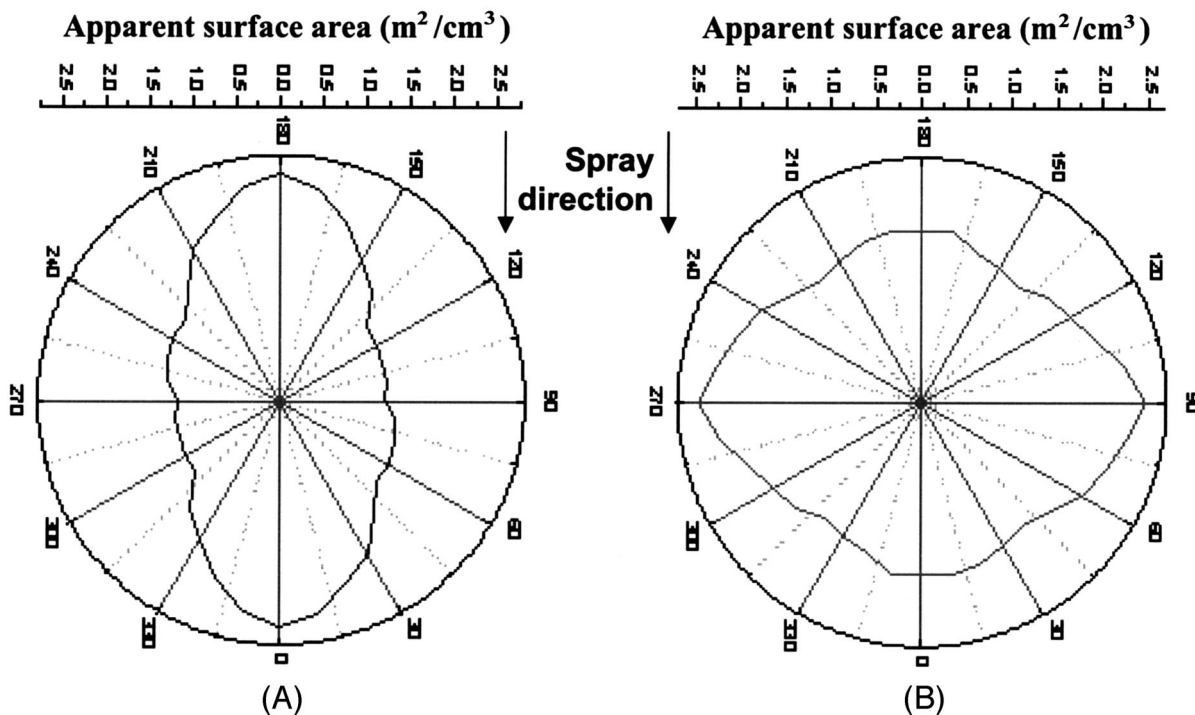


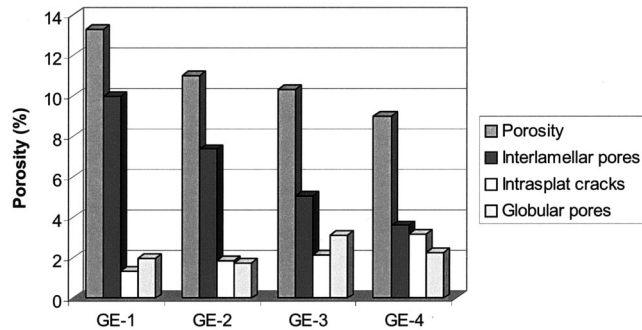
Fig. 3. Porod surface area anisotropy plots for (A) GE-1 and (B) GE-4 coatings.

Table II. Quantitative MSANS Model Results along with Orientation Information

Material	Porosity (%)	Component porosities (%)			Mean opening dimensions (μm)	Globular pore diameter (μm)
		Interlamellar pores	Intrasplat cracks	Globular pores		
GE-1	13.3 ± 0.3	9.9(8)	1.4(3)	1.9(9)	0.067	0.43(8)
GE-2	11 ± 0.2	7.4(7)	1.8(7)	1.8(6)	0.06	0.39(2)
GE-3	10.3 ± 0.2	5.1(5)	2.1(6)	3.1(2)	0.071	0.46(2)
GE-4	9 ± 0.2	3.6(1)	3.1(5)	2.2(5)	0.066	0.42(9)

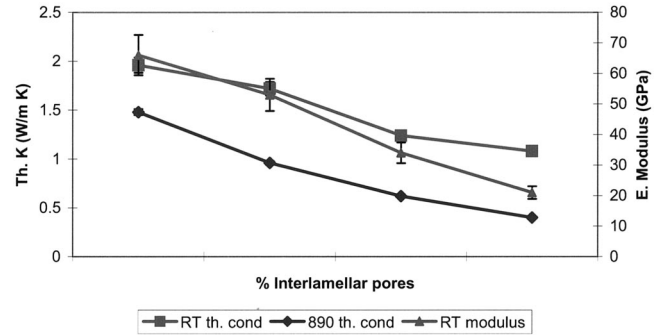
  

	GE-1		GE-4	
	Cracks (%)	Pores (%)	Cracks (%)	Pores (%)
(0°–30°)	4.5	95.2	9.3	87.6
(30°–60°)	12.2	3.5	12.7	11.5
(60°–90°)	83.3	1.3	78	0.9



**Fig. 4.** Quantitative separation of the total porosity, obtained from MSANS analysis, for each of the four samples.

(spheroidal-elements normals  $0\text{--}30^\circ$  from the spray direction). The quantitative separation of the coating microstructure into its components, obtained from the MSANS model, is shown in Fig. 4. It is seen that the component porosities of interlamellar pores decrease, from GE-1 to GE-4, thus enabling a correlation with the thermal conductivity and elastic modulus of the coatings. The component porosities of intrasplat cracks increase monotonically from GE-1 to GE-4, thereby explaining the decrease in cross-sectional modulus for the DVC coating. The porosity–thermal conductivity and porosity–elastic modulus correlations can be better understood in terms of the percentage of interlamellar pores in the coatings, as shown in Fig. 5. The behavior is very similar to the thermal conductivity values measured both at room temperature and at  $890^\circ\text{C}$ , where the lower value at  $890^\circ\text{C}$  occurs due to greater phonon scattering occurring at high temperature than at room temperature.



**Fig. 5.** Thermal conductivity (left ordinate) and out-of-plane elastic modulus (right ordinate) correlated with interlamellar porosity derived from MSANS. The vertical bars are the standard deviations on the mean of 10 measurements of each sample.

The USAXS measurements giving the pore size distributions for the two extreme cases (GE-1 and GE-4) are presented in Fig. 6. The scattering intensity as a function of azimuthal angle for the wave vector  $Q = 0.00038 \text{ \AA}^{-1}$  is presented for both cases and compared with the observed microstructural features. The plot for sample GE-1 shows dominant scattering from interlamellar pores in the coating. The intensity for GE-4 shows contributions from both vertical and horizontal components of the porosity in the coating. The combination of scattering data collected as a function of  $Q$  for each orientation and as a function of orientation at a particular  $Q$  provides quantitative maps of the anisotropy of the microstructure as a function of sizes within the scattering population for the two coatings, as shown in Fig. 7. For each sample, the maximum entropy size distribution (MAXENT) routine gives size

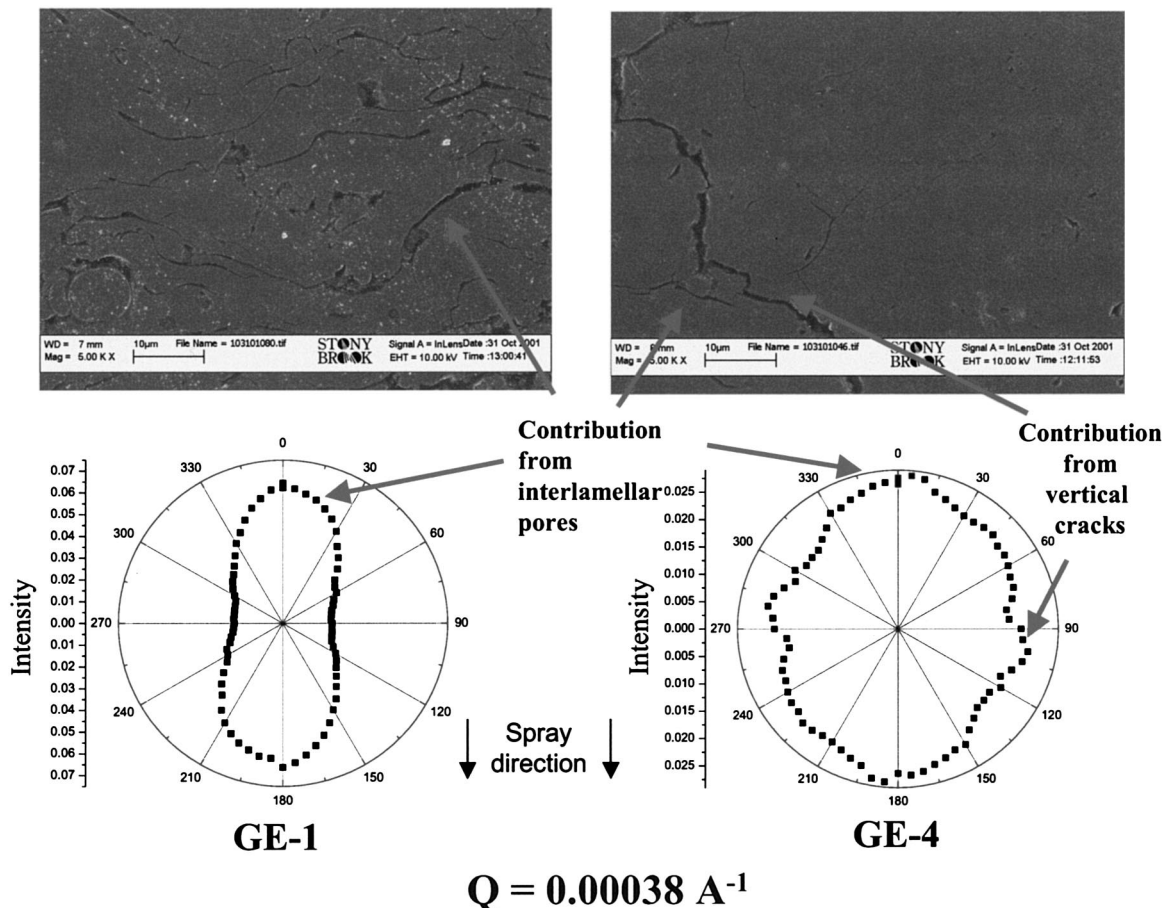


**Fig. 6.** Scattering intensity as a function of azimuthal angle  $\alpha$  for the GE-1 and GE-4 coating at  $Q = 0.00038 \text{ \AA}^{-1}$ . The errors are within the sizes of the data points.

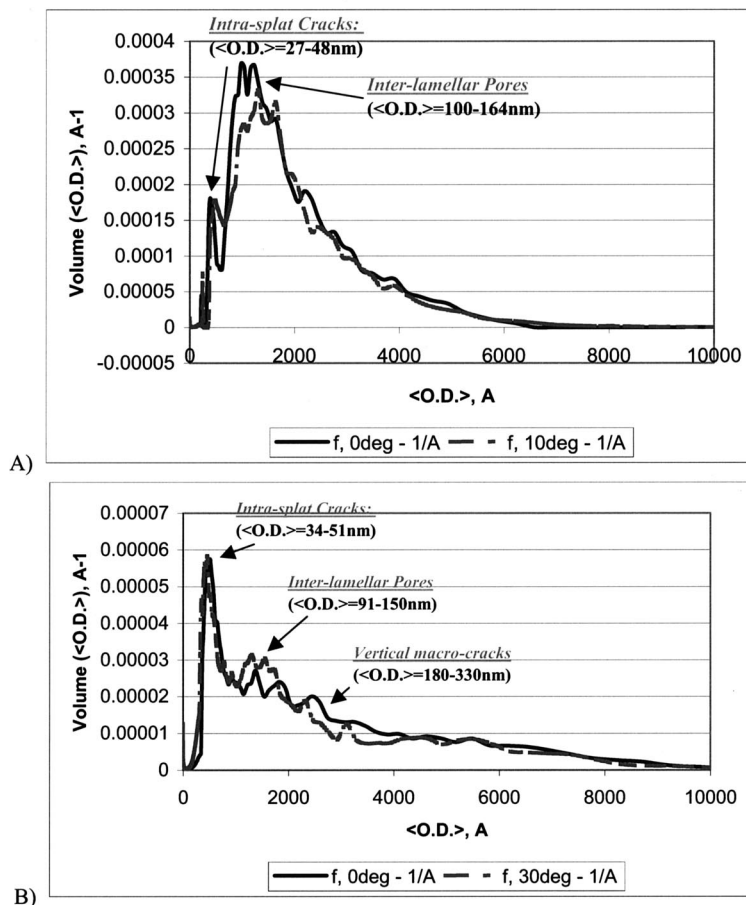


**Fig. 7.** MAXENT volume fraction size distributions of the coatings, for two orientations ( $\alpha$ ) with respect to the spray direction: (A) GE-1 coating showing interlamellar pores as the dominant system and (B) GE-4 coating showing a crack-dominant system.

distributions (no volume fraction contributions) of the void components that vary for different orientations of  $Q$  with respect to the spray direction. These differences arise from the anisotropy in the scattering and result from an assumption of random orientation distributions in the MAXENT routine.<sup>19,20</sup> It is envisaged that future work will extend the MAXENT routine to deal with nonrandom orientation distributions. However, in the present study, these discrepancies with orientation are not sufficient to detract from a comparison of the size distributions from different samples. It is seen that different features dominate the anisotropy at different magnitudes of  $Q$ . The results show an interlamellar pore dominant system for the GE-1 case in Fig. 7(A) as opposed to a crack dominant system for the GE-4 case in Fig. 7(B). The size ranges of the intrasplat cracks and interlamellar pores were similar in both systems. The analysis shows the opening dimension for interlamellar pores to be between 90 and 150 nm and that for the intrasplat cracks to be between 27 and 50 nm. Also observed are vertical macrocracks with opening dimensions between 180 and 330 nm in the GE-4 (DVC) case. The aspect ratio was assumed as 1/10 for both the interlamellar pores and intrasplat cracks, similar to the SANS model assumption. While this is not the true aspect ratio of macrocracks seen in the DVC micrographs, this spheroidal shape assumption gives us a way to deduce the volume fractions, opening dimensions, and orientation distributions. The assumption works because the scattering in this range is sensitive to the short area dimensions, and not particularly sensitive to the large area dimensions.

#### IV. Conclusions

The drive to develop these prime-reliant TBCs has fostered growing interest in comprehensive materials characterization for

establishing processing–structure–property relationships. It has been successfully demonstrated that SANS, in combination with USAXS and microscopy, has provided a quantitative representation of the different void components within plasma-sprayed deposits. The paper presents valid results of scientific characterization techniques to thin coatings of engineering importance. Complete microstructural information of constituent porosities, opening dimensions, along with orientation information of void morphologies sought using SANS, complemented by void size distribution obtained using USAXS, have led to rational porosity–property correlations. The studies show DVCs with the dominant vertical crack network system, depicting low in-plane modulus, to fall between traditional plasma sprayed (layered structures) and EB-PVD (columnar structures), thus offering optimization of processing economics, appropriateness, and performance.

#### Acknowledgments

The authors wish to thank Dr. Sanjay Sampath of SUNY Stony Brook for valuable discussions, Dr. Boualem Hammouda of the NIST Center for Neutron Research, and Dr. Pete Jemian of the Advanced Photon Source for scientific and technical support. We acknowledge the support of the National Institute of Standards and Technology, U.S. Department of Commerce, in providing the neutron research facilities used in this work.

#### References

- 1R. A. Miller, "Current Status of Thermal Barrier Coatings—An Overview," *Surf. Coat. Technol.*, **30**, 1–11 (1987).
- 2W. J. Brindley and R. A. Miller, "TBCs for Better Engine Efficiency," *Adv. Mater. Proc.*, **8**, 29–33 (1989).
- 3S. M. Meier and D. K. Gupta, "The Evolution of Thermal Barrier Coatings in Gas Turbine Applications," *J. Eng. Gas Turbines Power*, **116**, 250–57 (1994).

<sup>4</sup>R. L. Jones, "Thermal Barrier Coatings"; p. 194 in *Metallurgical and Protective Coatings*. Edited by K. H. Stern. Chapman and Hall, London, U.K., 1996.

<sup>5</sup>K. D. Sheffler and D. K. Gupta, "Current Status and Future Trends in Turbine Application of Thermal Barrier Coatings," *J. Eng. Gas Turbines Power*, **110**, 605–609 (1988).

<sup>6</sup>W. Mannsmann and H. W. Grunling, "Plasma Sprayed TBC for Industrial Gas Turbines: Morphology, Processing, and Properties," *J. Phys. IV*, **3**, 903–12 (1993).

<sup>7</sup>H. Herman, "Plasma Sprayed Coatings," *Sci. Am.*, **259** [3] 112–15 (1988).

<sup>8</sup>R. McPherson, "The Relationship Between the Mechanisms of Formation, Microstructure, and Properties of Plasma Sprayed Coatings," *Thin Solid Films*, **83**, 297–303 (1981).

<sup>9</sup>P. Bengtsson, T. Ericsson, and J. Wigren, "Thermal Shock Testing of Burner Cans Coated with a Thick Thermal Barrier Coating," *J. Therm. Spray Technol.*, **7** [3] 340–48 (1998).

<sup>10</sup>Gray, D. M.; Lau, Y. C.; Johnson, C. A.; Borom, M. P.; Nelson, W. A. (General Electric Co.). Thermal Barrier Coatings Having an Improved Columnar Microstructure. U.S. Patent 6,180,184, October 24, 1997.

<sup>11</sup>A. Kulkarni, A. Vaidya, A. Goland, S. Sampath, and H. Herman, "Processing Effects on Porosity–Thermal Conductivity Correlations in Plasma Sprayed Yttria-Stabilized Zirconia Coatings," *Mater. Sci. Eng., A*, **359**, 100–111 (2003).

<sup>12</sup>S. Sampath and X. Jiang, "Splat Formation and Microstructure Development During Plasma Spraying: Deposition Temperature Effects," *Mater. Sci. Eng. A*, **304–306**, 144–50 (2001).

<sup>13</sup>S. Sampath, X. Y. Jiang, J. Matejcek, A. C. Leger, and A. Vardelle, "Substrate Temperature Effects on Splat Formation, Microstructure Development and Properties

of Plasma Sprayed Coatings: Part I, Case Study for Partially Stabilized Zirconia," *Mater. Sci. Eng. A*, **272** [1] 181–88 (1999).

<sup>14</sup>J. Ilavsky, A. J. Allen, G. G. Long, S. Krueger, C. C. Berndt, and H. Herman, "Influence of Spray Angle on the Pore and Crack Microstructure of Plasma Sprayed Deposits," *J. Am. Ceram. Soc.*, **80**, 733–42 (1997).

<sup>15</sup>A. J. Allen, J. Ilavsky, G. G. Long, J. S. Wallace, C. C. Berndt, and H. Herman, "Microstructural Characterization of Yttria-stabilized Zirconia Plasma-Sprayed Deposits Using Multiple Small-Angle Neutron Scattering," *Acta Mater.*, **49**, 1661–75 (2001).

<sup>16</sup>A. J. Allen and N. F. Berk, "Analysis of Small-Angle Scattering Data Dominated by Multiple Scattering for Systems Containing Eccentrically Shaped Particles or Pores," *J. Appl. Crystallogr.*, **27**, 878–91 (1994).

<sup>17</sup>U. Bonse and M. Hart, "A New Tool for Small-Angle X-ray Scattering and X-ray Spectroscopy: The Multiple Reflection Diffractometer," *Appl. Phys. Lett.*, **7**, 238–40 (1965).

<sup>18</sup>J. Ilavsky, A. J. Allen, G. G. Long, and P. R. Jemian, "Effective Pinhole-Collimated Ultrasmall-Angle X-ray Scattering Instrument for Measuring Anisotropic Microstructures," *Rev. Sci. Instrum.*, **73** [3] 1660–62 (2002).

<sup>19</sup>J. A. Potton, G. J. Daniell, and B. D. Rainford, "Particle Size Distribution from SANS Data Using the Maximum Entropy Method," *J. Appl. Crystallogr.*, **21**, 663–68 (1988).

<sup>20</sup>G. G. Long, S. Krueger, P. R. Jemian, D. R. Black, H. E. Burdette, J. P. Cline, and R. A. Gerhardt, "Small-Angle Scattering Determination of the Microstructure of Porous Silica Precursor Bodies," *J. Appl. Crystallogr.*, **23**, 535–44 (1990). □